RESEARCH ARTICLE

Key Points:
- SAMPEX/HILT observes microburst and band-type rapid precipitation events
- Relative role of these loss processes is examined across MLT, L, and storm phase
- Significant radiation belt electron precipitation is observed during HSS storms

Correspondence to:
L. Blum,
lwblum@ssl.berkeley.edu

Rapid MeV electron precipitation as observed by SAMPEX/HILT during high-speed stream-driven storms

Lauren Blum[1,2], Xinlin Li[1], and Mick Denton[3]

[1]Laboratory for Atmospheric and Space Physics and Department of Aerospace Engineering Sciences, University of Colorado Boulder, Boulder, Colorado, USA, [2]Now at Space Sciences Laboratory, University of California, Berkeley, California, USA, [3]Space Science Institute, Boulder, Colorado, USA

Abstract A number of relativistic electron loss processes exist in the inner magnetosphere, and the extent to which MeV electron precipitation into Earth's atmosphere plays a role in radiation belt dynamics is a topic of much debate. In this work, we investigate the contribution of electron precipitation to radiation belt losses, looking at what times and locations precipitation is important. Through high-cadence low-altitude measurements from the Solar, Anomalous, and Magnetospheric Particle Explorer (SAMPEX) satellite, we examine the distributions of millisecond (microburst) as well as longer-duration (band-type) precipitation and the relative contributions of these two precipitation types to radiation belt dynamics during high-speed stream (HSS)-driven storms. Different local time and radial distributions between microbursts and precipitation bands suggest different scattering mechanisms as the causes of the two precipitation types. In a superposed epoch study of 42 HSS-driven storms, enhanced main and recovery phase losses to the atmosphere are observed. Microburst occurrence rates peak in the recovery phase of the storms, while their magnitudes remain fairly constant over storm phase. Precipitation bands show an increase in both occurrence and magnitude at storm onset, particularly at the inner edge of the outer radiation belt. The observations, enabled by the high time resolution and large geometric factor and field of view of the SAMPEX/Heavy Ion Large Telescope (HILT) instrument, reveal when and where microburst and band-type precipitation are contributing to radiation belt dynamics during HSS-driven storms.

1. Introduction

Earth's outer radiation belt is a highly dynamic region of the magnetosphere, composed of relativistic electrons with often unpredictable variations in energy and spatial extent. A number of competing acceleration and loss processes combine to produce net enhancements or depletions of the outer radiation belt [*Li and Temerin*, 2001; *Friedel et al.*, 2002; *Liemohn and Chan*, 2007]. Electron precipitation into the atmosphere is a critical part of this loss, and quantified understanding of this process is needed in order to understand and ultimately predict radiation belt dynamics. The slow decay of the outer radiation belt observed during quiet times has been attributed to slow, steady pitch angle diffusion by plasmaspheric hiss waves, resulting in electron lifetimes on the order of 5–20 days [*Meredith et al.*, 2006]. However, changes in the trapped outer belt electron population often occur on much faster timescales as well, particularly in response to geomagnetic activity [e.g., *Reeves et al.*, 2003]. Rapid depletions of outer belt electrons following geomagnetic storms are often not fully explained by losses to the magnetopause and outward diffusion [e.g., *Hudson et al.*, 2014; *Turner et al.*, 2014], suggesting that other mechanisms including rapid atmospheric loss must be occurring as well.

The response of the outer radiation belt to high-speed stream (HSS)-driven storms in particular has been studied in great detail [e.g., *Li et al.*, 1997a; *Denton and Borovsky*, 2008; *Borovsky and Denton*, 2009a, 2009b; *Denton et al.*, 2010]. These storms produce characteristic flux dropouts during the main phase, followed by a building back up of the outer belt in subsequent days to often larger fluxes than prestorm levels [*Miyoshi and Kataoka*, 2008]. The onset of these relativistic electron dropouts is coincident with onset time of storm convection, as measured by a rise in the *Kp* index, and occurs in the main phase of the storms as the *Dst* index is decreasing [*Borovsky and Denton*, 2009a]. A number of studies have attempted to determine the cause or causes of these dropouts. *Morley et al.* [2010] find that the magnetopause remains beyond ~8 R_E during a set of HSS in 2005–2008 and suggest that mechanisms other than losses to this outer boundary

are responsible for the flux dropouts seen across the entire outer belt, down to L shells of ~3. They suggest, based on energetic electron precipitation signatures in the morning sector inferred from riometer measurements, that chorus-driven microburst precipitation may be a main contributor to HSS-driven storm time losses but does not necessarily account for the rapid main phase dropouts. [*Sandanger et al.*, 2008] find evidence for electromagnetic ion cyclotron (EMIC) wave-driven electron scattering and precipitation occurring at all local times throughout three case study storms investigated, and *Borovsky and Denton* [2009a] propose that dropouts observed at geosynchronous satellites during a set of 124 HSS-driven storms may be due to EMIC waves generated by the overlap of plasmaspheric drainage plumes and a superdense plasma sheet. However, *Meredith et al.* [2011] look at precipitating electrons observed by POES satellites at low Earth orbit (LEO) during a similar set of HSS storms in 2003–2005 and find little indication of enhanced storm time MeV electron loss to the atmosphere. Finally, *Hendry et al.* [2012], using a combination of riometers and narrowband subionospheric ground-based VLF receivers, part of the Antarctic-Arctic Radiation-belt Dynamic Deposition VLF Atmospheric Research Konsortia [*Clilverd et al.*, 2009] and sensitive to precipitation of approximately tens to hundreds of keV electrons, find that the precipitating flux inferred by ground measurements can be ~10 times larger than that observed by POES. Thus, the question remains as to the extent of MeV electron precipitation during HSS-driven storms and the impact of this on radiation belt dynamics.

Here we investigate MeV electron precipitation during HSS-driven storms as observed by Solar, Anomalous, and Magnetospheric Particle Explorer (SAMPEX) Heavy Ion Large Telescope (HILT) [*Klecker et al.*, 1993]. Low-altitude measurements, such as those from SAMPEX, are necessary to make direct measurements of precipitation loss, as most low-inclination, high-altitude spacecraft cannot resolve the electron pitch angle distribution near and inside the loss cone. We focus on two distinct types of rapid precipitation often observed at LEO: millisecond-long "microbursts" and longer-duration "precipitation bands" (described in detail in section 2). Each of these precipitation signatures has been shown to be able to produce substantial radiation belt electron losses on timescales of hours [*O'Brien et al.*, 2004; *Thorne et al.*, 2005; *Blum et al.*, 2013]. The distributions of these rapid precipitation features are analyzed here as a function of magnetic local time (MLT), L shell, and storm phase during 42 HSS-driven storms. With its large field of view and geometric factor, as well as high time resolution measurements, we look to investigate if SAMPEX/HILT can reveal anything more regarding precipitation losses during HSS-driven storms. By focusing on specific types of precipitation, and investigating the distributions of these rapid precipitation events, we gain insight into the relative roles of various loss processes with respect to the flux dropouts and subsequent enhancements often observed in the outer radiation belt in response to HSS-driven storms.

2. SAMEPX/HILT Observations

SAMPEX was launched in July 1992 into a 520–670 km, 82° inclination orbit [*Baker et al.*, 1993]. Initially expected to reenter the atmosphere by 2000, a quiet Sun and extended solar minimum allowed it to remain in operation until November 2012 [*Baker et al.*, 2012]. The HILT (Heavy Ion Large Telescope) instrument on board SAMPEX contains an array of 16 solid-state detectors (SSDs) arranged in four rows of four, each row with its own signal-processing chain and labeled SSD1–SSD4 [*Blake et al.*, 1996]. The HILT instrument has a view angle of 68° × 68° and geometric factor of ~60 cm^2 sr (15 cm^2 sr per row) [*Klecker et al.*, 1993]. The instrument was operated in four different modes over the course of the mission, returning anywhere between 20 and 100 ms count rates of > 1 MeV electrons in one to four of these rows.

The equatorial loss cone in the outer radiation belt is < ~6°, making it difficult to resolve precipitating fluxes from low-inclination orbits. At low altitudes, however, this loss cone opens up to values of ~60° and greater, allowing SAMPEX to directly measure electrons within and just outside the loss cone. Due to the offset, asymmetric nature of Earth's internal magnetic field, the size of this loss cone varies with both longitude and hemisphere. Particles can thus be categorized as one of three types: ones that will be lost to the atmosphere within one bounce period (untrapped or bounce loss cone, BLC), ones that are lost within one drift period (quasi-trapped or drift loss cone, DLC), and those that remain trapped in the magnetosphere for timescales longer than their drift period. With its wide, 68° field of view, SAMPEX/HILT measures a combination of these three particle populations at different points along its orbit [see *Dietrich et al.*, 2010, Figure 3]. Measurements around the South Atlantic Anomaly (SAA), a region of lower magnetic field
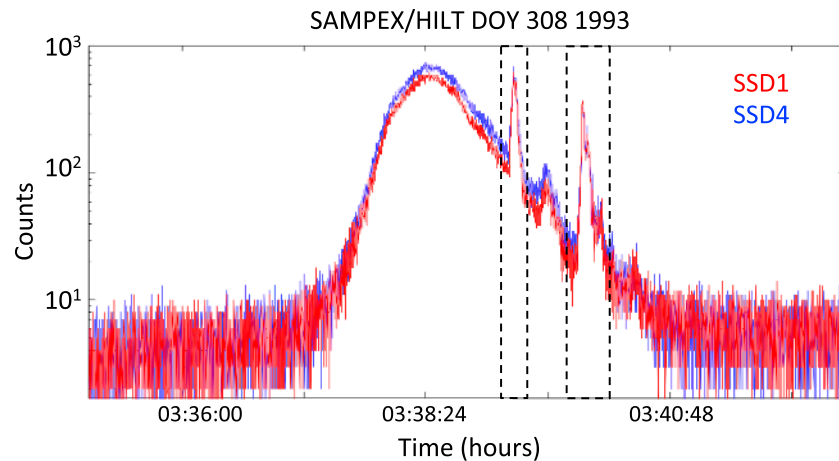
Figure 1. SAMPEX/HILT data from the SSD1 (red) and SSD4 (blue) detector rows during a pass through the outer radiation belt. Qualitative pitch angle information can be obtained by comparing the count rates in these two detector rows. More anisotropic, 90° peaked populations are observed throughout most of the outer radiation belt, while the count rates converge during rapid precipitation events shown in the dashed rectangles.

strength above the coast of Argentina, are dominated by trapped particles, while any electrons measured by SAMPEX at conjugate locations in the Northern Hemisphere will precipitate within one bounce.

To help distinguish among these three particle populations, BLC, DLC, and trapped, in the HILT data, qualitative pitch angle information can be extracted by comparing the count rates in SSD1 to SSD4. The HILT instrument is roughly zenith pointing, with an angle ≤30° with respect to the background magnetic field, at latitudes corresponding to the outer radiation belt [*Blake et al.*, 1996]. Due to the detector rows' slightly different look directions with respect to the magnetic field, they measure slightly different local pitch angle ranges. A difference in the count rates between SSD1 and SSD4 suggests a more anisotropic distribution and measurements dominated by trapped and quasi-trapped electrons. In contrast, an isotropic distribution is indicated when all four SSD count rates converge to the same value [*Blake et al.*, 1996]. While the HILT measurements tend to be anisotropic and dominated by trapped and quasi-trapped particles as SAMPEX passes through the outer belt, at certain times rapid pitch angle scattering occurs, filling the bounce loss cone and causing direct precipitation. When measured by the SAMPEX/HILT instrument, these events appear as rapid flux increases with an accompanying isotropization of the flux, superimposed atop the smoothly varying background anisotropic trapped and drift loss cone fluxes, as depicted in Figure 1. The following sections describe two distinct types of rapid precipitation events seen in the SAMPEX/HILT data—microbursts and precipitation bands. Previous studies have shown that both microbursts and precipitation bands are characterized by more isotropic fluxes that fill the loss cone [*Blake et al.*, 1996; *Li et al.*, 1997b], as shown in Figure 1, indicative of rapid local precipitation rather than simply an increase in the trapped population at these times.

2.1. Microbursts

Rapid bursts of electron precipitation lasting <1 s were first observed by balloon-borne detectors in 1964 [*Anderson and Milton*, 1964]. These observations were of tens to hundreds of keV electrons, and similar bursts were subsequently seen by low-altitude satellites as well. The first similar duration (~100 ms) relativistic electron (>1 MeV) precipitation bursts were detected by the low-altitude, Sun-synchronous S81-1 satellite [*Imhof et al.*, 1992]. These relativistic microbursts have been seen by a number of low-altitude satellites since then, including SAMPEX, and are the precipitation features of interest here as our focus is on MeV electron dynamics. They occur most frequently on the dawn side during periods of enhanced geomagnetic activity [*Nakamura et al.*, 2000; *Lorentzen et al.*, 2001]. Their consistently sharp rise times and slower decay suggest that the bursts are temporal, typically lasting on the order of 100 ms [*Millan and Thorne*, 2007]. Estimates of the physical size of individual microbursts are on the order of 10 km [*Blake et al.*, 1996; *Dietrich et al.*, 2010], while the process generating the bursts likely spans a significantly larger area

BLUE: 100 ms count rate
RED: Baseline - 10th percentile of 3 sec bins

BLUE: 100 ms count rate
RED: Band detections
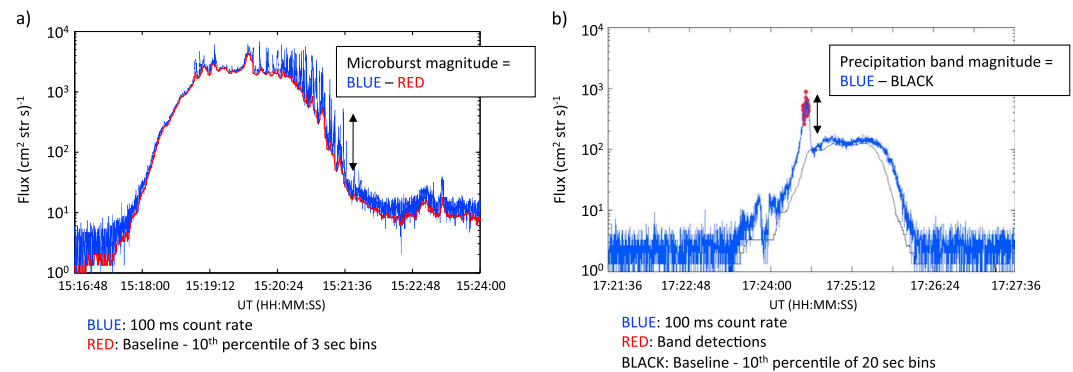BLACK: Baseline - 10th percentile of 20 sec bins

Figure 2. SAMPEX/HILT >1 MeV electron measurements during two passes through the outer radiation belt, each lasting ~5 min. Rapid enhancements in the measured count rates are visible in (a) millisecond and (b) longer-duration timescales. Results of an automated detection and magnitude calculation algorithm for microbursts (Figure 2a) and precipitation bands (Figure 2b) are shown as well.

[*Lorentzen et al.*, 2001; *Dietrich et al.*, 2010]. Microbursts are often measured in groups or clumps (see Figure 2a), but the spatial and temporal extents of these regions of microburst activity are still uncertain [*Spence et al.*, 2012].

Whistler mode chorus waves are a primary mechanism believed to produce microburst precipitation. Similar distributions in local time and L shell between the waves and precipitation features suggest that the two phenomena are likely related [*Lorentzen et al.*, 2001]. *Johnston and Anderson* [2010] found that microburst distributions are well-constrained to outside the plasmapause boundary, in good agreement with chorus wave distributions as well [*Tsurutani and Smith*, 1977]. Theoretical calculations show that whistler mode chorus waves, gyroresonant with the keV electrons near the equator, can resonate with MeV electrons at higher latitudes or higher-order harmonics of the gyrofrequency [*Horne and Thorne*, 2003; *Thorne et al.*, 2005]. Simulations by *Saito et al.* [2012] also indicate that relativistic microbursts can be produced by rising-tone elements of whistler chorus waves propagating to high magnetic latitudes. Large-amplitude whistler waves propagating obliquely to the background magnetic field, first reported by *Cattell et al.* [2008], have also been suggested as scattering mechanisms through nonlinear wave-particle interactions. *Kersten et al.* [2011] observed MeV microbursts at SAMPEX in close conjunction with large-amplitude obliquely propagating whistler waves measured by Wind and STEREO spacecraft. Additionally, electrostatic upper hybrid resonance waves, which also occur outside the plasmapause, have been demonstrated to be capable of producing MeV electron microburst precipitation, perhaps at stronger scattering rates than high-latitude chorus waves [*Shklyar and Kliem*, 2006].

Using SAMPEX/HILT measurements, *O'Brien et al.* [2004] and *Lorentzen et al.* [2001] estimate microburst losses to be capable of emptying the entire relativistic electron content of the outer radiation belt during a storm. *Thorne et al.* [2005] calculate radiation belt electron lifetimes due to microbursts to be on the order of 1 day during the main phase of geomagnetic storms, suggesting that these events can contribute significantly to storm time losses. However, whistler mode chorus waves have been proposed as both a potential source of microbursts and a strong local acceleration mechanism in the outer radiation belt [*Bortnik and Thorne*, 2007]. For this reason, microbursts have been used both as a measure of radiation belt electron loss and additionally as a proxy for chorus wave activity and acceleration of electrons [*O'Brien et al.*, 2003]. The balance of this loss and acceleration, both potentially caused by chorus waves, contributes to the overall dynamics of the outer radiation belt.

2.2. Precipitation Bands

A second distinct type of rapid precipitation seen in SAMPEX data are broader, typically a few degrees in latitude, and are referred to here as precipitation bands following *Blake et al.* [1996]. These bands are often seen in conjugate locations and on consecutive orbits [*Blake et al.*, 1996], suggesting that their tens of seconds duration (as measured by LEO satellites) is due to spatial rather than temporal characteristics. *Blum et al.* [2013] have shown that precipitation bands can last up to hours and contribute significantly to

loss of electrons from the outer radiation belt. Figure 2b depicts an example precipitation band measured around 17:24:30 UT, corresponding to an L shell of 5.5, as SAMPEX cuts through the outer radiation belt, moving from larger to smaller L shells.

Precipitation bands have been observed during both quiet and more active times, spanning the afternoon and nighttime sectors [*Brown and Stone*, 1972; *Nakamura et al.*, 2000]. It has been suggested that precipitation bands observed during quiet times may be associated with electrostatic waves or the trapping limit [*Vampola*, 1971; *Koons et al.*, 1972; *Vampola*, 1977; *Imhof et al.*, 1991], while those during more active times may be induced by electromagnetic ion cyclotron (EMIC) waves [*Thorne and Kennel*, 1971; *Vampola*, 1977; *Bortnik et al.*, 2006]. Theory has shown that EMIC waves are able to resonate with both keV ions and MeV electrons, breaking their first adiabatic invariant and scattering the particles into the loss cone [*Albert*, 2003; *Summers and Thorne*, 2003]. In the inner magnetosphere, these waves are observed primarily in the afternoon sector, where anisotropic ring current ions overlap cool, dense plasmaspheric plumes [*Fraser and Nguyen*, 2001; *Spasojevic et al.*, 2004; *Clausen et al.*, 2011]. EMIC waves can also be generated at larger radial distances under strong solar wind dynamic pressure, compressing the magnetopause and generating ion anisotropy across the dayside [*McCollough et al.*, 2012; *Usanova et al.*, 2012]. However, as the outer radiation belt rarely extends beyond L ~ 7, it is the EMIC wave distributions within geosynchronous orbit that are most directly relevant for MeV electron precipitation studies. EMIC wave occurrence rates in the inner magnetosphere peak during the main phase of storms but often persist into the recovery phase as well [*Bossen et al.*, 1976; *Halford et al.*, 2010]. *Imhof et al.* [1986] found a correspondence between the radial location of the plasmapause and precipitation bands, as well as keV ion precipitation concurrent with MeV electron precipitation during some events, a signature commonly interpreted as due to EMIC wave scattering [e.g., *Sandanger et al.*, 2007].

2.3. Automated Identification

The first step toward investigating the storm time distributions of these rapid precipitation events was to identify the microbursts and precipitation band features in the SAMPEX data set and construct a database to provide the framework for statistical studies. The features are identified based on their distinct durations and profiles: microbursts appearing as sharp spikes lasting less than a second and precipitation bands as rapid enhancements in flux often remaining elevated for ~5–30 s. As previous work has shown that these features are associated with flux isotropization and precipitation [*Blake et al.*, 1996; *Li et al.*, 1997b], we identify them here based only on the rapid enhancement profile in SSD4, rather than by also comparing SSD1 and SSD4 count rates. SSD4 measurements were used as they are available throughout the majority of the mission, while other detector rows, or combined/averaged count rates, are provided as a data product only during some instrument operation modes. As SSD1 and SSD4 are alternately measuring higher and lower fluxes during anisotropic distributions, the statistical patterns investigated here would be similar if a different detector row were used.

We have identified the microbursts using the following burst criterion developed by *O'Brien et al.* [2003]:

$$(N_{100} - A_{500})/\sqrt{1 + A_{500}} > 10$$

where N_{100} is the number of counts in 100 ms and A_{500} is a running average over 500 ms. Microburst magnitudes are then extracted by taking the difference between N_{100} and a baseline flux, B_3, defined as the 10th percentile in 3 s bins. Requiring this expression to be >10 sets a lower bound on the microburst magnitudes able to be identified; we have performed sensitivity tests and find that the current value of 10 picks up most microbursts while minimizing false detections. Furthermore, by using the same criteria as past studies [e.g., *O'Brien et al.*, 2003], we are better able to compare our results to theirs.

An algorithm was developed for this study to detect precipitation bands in the 100 ms SAMPEX/HILT data as well. We require (1) $N_{100} > 4 \times B_{20}$ for ≥5 s and (2) the 10 s linear correlation coefficient between N_{100} and B_{20} to be less than 0.955, where B_{20} is the 10th percentile in 20 s bins. Magnitudes are defined by the difference between N_{100} and B_{20}. The correlation coefficient requirement eliminates false detections from rapidly rising (falling) fluxes as the satellite enters (exits) the outer radiation belt. Parameter studies have been performed on these detection criteria as well, varying the required magnitude above baseline, duration of the enhancement, calculation of background baseline values, and correlation coefficient requirement. The final criteria used here have been tuned to reduce false positives; however, this causes some smaller band
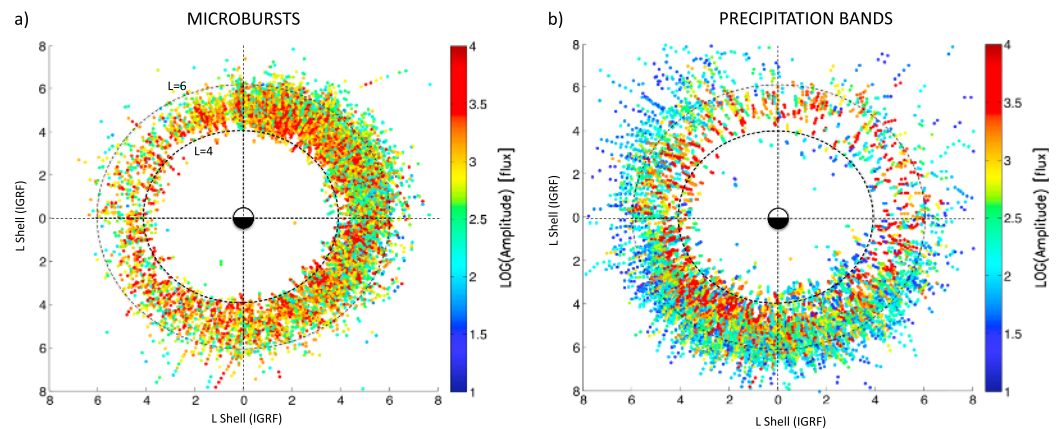
Figure 3. Distributions of (a) microbursts and (b) precipitation bands in L shell and magnetic local time (MLT) as measured by SAMPEX/HILT from 2003 to 2005. Precipitation magnitude is shown in the color scale. The events are searched for within the same data set, so local time differences between the two precipitation types are not due to sampling. Local noon is at the top.

events to go undetected. While the overall occurrence rates calculated using these detection criteria may be lower estimates, the patterns in occurrence as well as magnitude across local time, storm phase, and L shell remained consistent when looser or tighter criteria were explored.

Figure 2 illustrates example results of these algorithms during two passes of SAMPEX through the outer radiation belt; the time, location, duration, and magnitude of the microbursts and precipitation bands are extracted via these automated procedures. With these two selection methods, we have created a database of both microbursts and precipitation bands from the SAMPEX/HILT SSD4 data. This database is then drawn from to investigate the spatial and storm time distributions of these two types of rapid precipitation.

3. Results: Local and Storm Time Distributions

Using the database of rapid precipitation events described above, the spatial and temporal distributions of microbursts and precipitation bands are investigated during HSS-driven storms. The spatial distributions of the precipitation events from 2003 to 2005, the period examined in the superposed epoch study described in the following section, are presented in Figure 3. The location and magnitude of microbursts (Figure 3a) and precipitation bands (Figure 3b) across MLT and L shell throughout this 3 year period are displayed, with local noon toward the top. Microbursts are clustered on the morning side, between midnight and noon, in agreement with past statistical findings [e.g., *Lorentzen et al.*, 2001]. Occurrences remain constrained primarily between L = 4 and L = 6, indicated by the dashed circles, and magnitudes vary across this whole region and all local times. The precipitation bands, on the other hand, occur primarily on the evening and nightside, again in good agreement with past band observations by other LEO satellites [e.g., *Imhof et al.*, 1986]. This agreement in spatial distribution between our findings and other studies helps to validate the automated precipitation band detection criteria. Precipitation band magnitudes are observed to peak between 18 and 24 MLT and drop off with increasing L. While there are fewer small-magnitude microbursts as compared to the precipitation bands, this is likely due to the selection criteria used here.

While other studies have investigated MeV precipitation events as well, selection criteria or the nature of the observations often differ, making it difficult to determine whether the same phenomena are being examined as the precipitation bands shown here. Balloon campaigns have observed relativistic electron precipitation, or "REP," at low altitude [*Foat et al.*, 1998; *Millan et al.*, 2007]. As compared to LEO satellites, which cut across L shells at ~7 km/s, balloon measurements are relatively stationary. The REP events last minutes to hours as seen by balloons, and while precipitation events were observed at all local times by the MeV Auroral X-ray Imaging and Spectroscopy (MAXIS) balloon campaign [*Millan et al.*, 2002], the harder energy spectrum MeV events occurred exclusively on the duskside. *Comess et al.* [2013] have also surveyed SAMPEX data for REP events, using data from only when the spacecraft was conjugate to the SAA and measuring purely bounce loss cone electrons, rather than selecting on band-like features in the data as is done in the current study. The *Comess et al.* [2013] REP events also have occurrence rates peaking on the duskside and
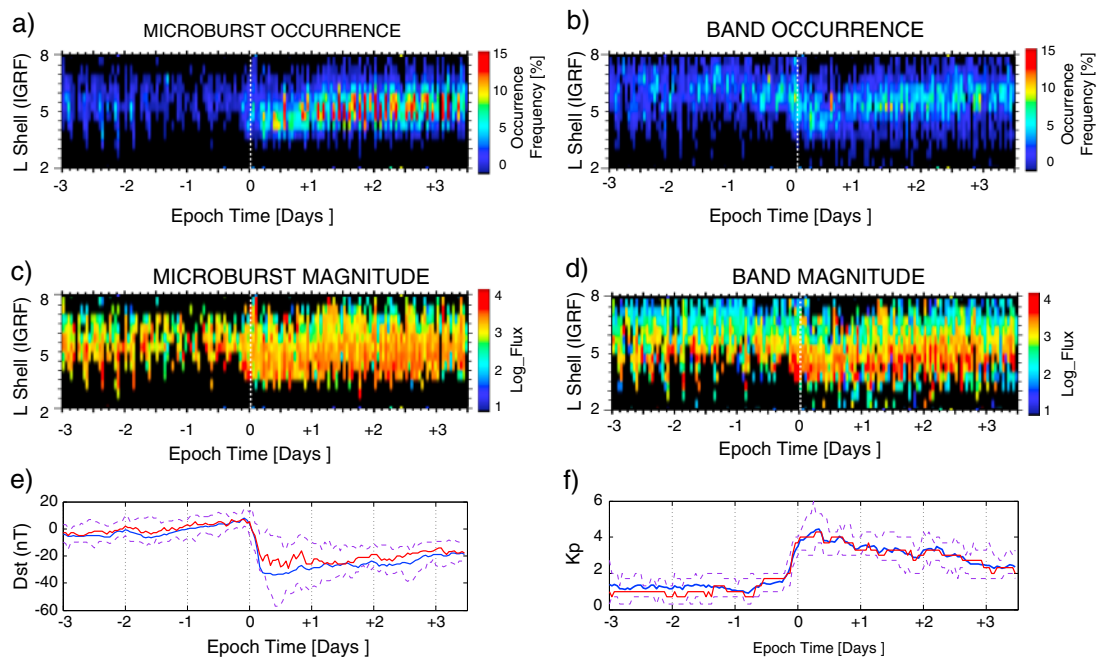
Figure 4. Superposed epoch results from 42 HSS-driven storms in 2003–2005. (a and b) Occurrence rates and (c and d) magnitudes are shown for microbursts (Figures 4a, 4c, and 4e) and precipitation bands (Figures 4b, 4d, and 4f) as functions of L shell and epoch time or storm phase. Superposed (e) Dst and (f) Kp indices are shown; mean values in blue, median values in red, and upper and lower quartiles by the dashed purple lines.

nightside. Finally, to investigate precipitation due primarily to EMIC waves, *Carson et al.* [2013] identified times when POES observed MeV electron precipitation concurrent with keV ion precipitation, a signature often associated with EMIC wave scattering [e.g., *Miyoshi et al.*, 2008]. The distributions they found peaked between dusk and midnight, similar to the SAMPEX precipitation bands shown in Figure 3b. These studies all suggest that MeV electron precipitation on timescales longer than microbursts occurs primarily on the duskside and that the duration of precipitation bands, as measured by SAMPEX/HILT, is likely due to spatial rather than temporal constraints.

There is a distinct difference in the spatial distributions of the two precipitation types shown in Figure 3, suggesting that these precipitation features are caused by different scattering mechanisms or wave modes. By isolating these two types of precipitation, we can now study how each contributes to overall precipitation throughout the course of HSS storms.

To study the storm time distributions of these two different precipitation types, a set of 42 high-speed stream-driven storms from 2003 to 2005 is investigated, taken from a larger list of HSS storms originally identified by *Denton and Borovsky* [2008] and subsequently studied by *Meredith et al.* [2011]. Using superposed epoch technique, we explore how the occurrence rates and magnitudes of microbursts and precipitation bands evolve over the course of the storms. Following *Denton and Borovsky* [2008], zero epoch time is set to the onset of strong magnetospheric convection, which accompanies the arrival of HSSs and is initially identified by a strong increase in the *Kp* index. This onset time is further refined beyond the 3 h *Kp* time resolution using the midnight boundary index [*Madden and Gussenhoven*, 1990]. Mean (in blue), median (red), and upper and lower quartile (dashed purple) values of *Dst* and *Kp* indices during these storms are shown in Figures 4e and 4f, respectively. Average Dst_{min} is ~ −35 nT and occurs roughly 0.5 days after zero epoch. During the storm main phase, the outer radiation belt electrons exhibit a dropout extending across all L shells, followed by a slow recovery over the next 4 days to fluxes somewhat higher than prestorm levels [see *Meredith et al.*, 2011, Figure 1].

Figure 4 shows the distributions of microbursts (a and c) and precipitation bands (b and d), as a function of epoch time and L shell, calculated using the International Geomagnetic Reference Field (IGRF) model, during these 42 HSS-driven storms. Occurrence rates of both precipitation types are shown in Figures 4a and 4b and precipitation magnitude directly below in Figures 4c and 4d. Microburst occurrence rates exhibit a dramatic
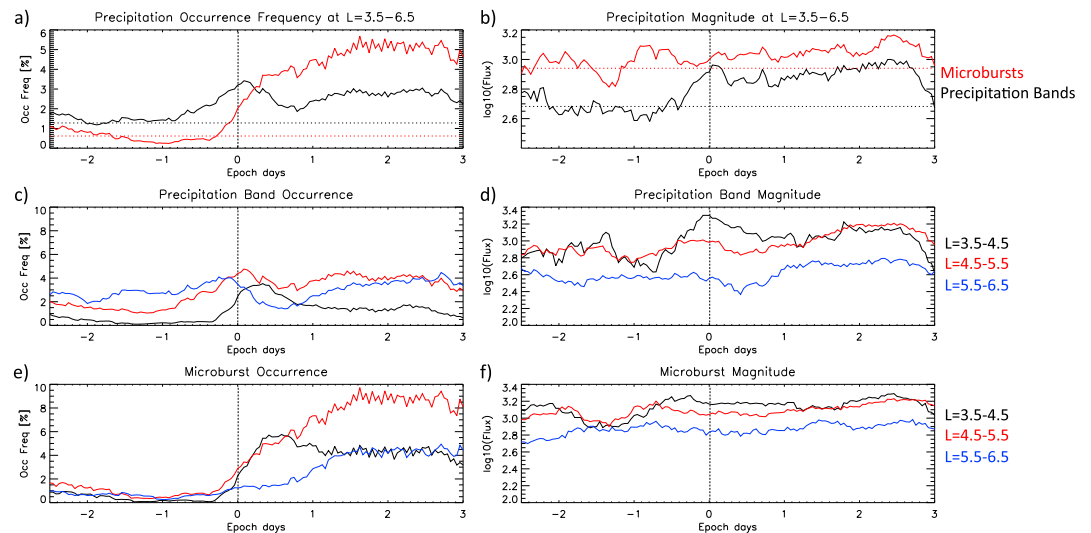
Figure 5. (a) Occurrence rates and (b) magnitudes of microbursts (red) and precipitation bands (black) averaged across the outer radiation belt, from L = 3.5–6.5. Precipitation band (c) occurrence rates and (d) magnitudes for the given L shell bins, indicated by color. Microbursts (e) occurrence rates and (f) magnitudes for the given L shell bins. Note that in Figures 5a and 5b the color indicates precipitation type, while in Figures 5c–5f it denotes different L shell ranges.

increase during the recovery phase period of the storms, while the magnitudes, on average, remain fairly independent of storm phase. The precipitation bands, on the other hand, show an increase in magnitude right around zero epoch, as well as through the recovery phase, at distances within L ~ 5. The radial location of both precipitation types moves inward around zero epoch, likely tracking the contraction of the plasmasphere prior to and during storm main phase [*Carpenter and Anderson*, 1992; *Goldstein et al.*, 2002].

4. Discussion

To more quantitatively investigate the variation in microburst and precipitation band distributions over radial distance and storm time, we examine the data shown in Figure 3 as a function of epoch time for specific ranges of L. Figure 5a shows occurrence rates of microbursts (red) and precipitation bands (black) versus epoch time averaged across the outer radiation belt, from L = 3.5–6.5. The dotted lines show prestorm averages of these values. Figures 5c and 5e show the occurrence rates for the given L shell bins, as indicated by color, for precipitation bands and microbursts, respectively. Precipitation magnitudes are shown in Figure 5b, in the same format as Figure 5a. Finally, in Figures 5d and 5f, average magnitudes for the given L shell bins are displayed for precipitation bands and microbursts, respectively.

Clear patterns are observable, indicative of the role that microburst and precipitation band losses play during HSS-driven storms. The microbursts show a significant increase in occurrence all across the outer radiation belt, beginning around zero epoch but ramping up over the subsequent few days to peak values of ~10% in the heart of the outer radiation belt at L ~ 5. These higher microburst occurrence rates persist through the recovery phase of the storms, as the trapped outer belt fluxes build back up. Microburst amplitudes, however, do not vary significantly over epoch time during these HSS-driven storms (see Figures 5b, 5f, and 6c), remaining at a roughly constant value of 10^3 (MeV cm^2 sr s)$^{-1}$. The large variations at L > 6.5 visible in Figure 6c are likely due to low occurrence rates at these distances. This roughly constant magnitude is in contrast to patterns observed by *O'Brien et al.* [2004], who found that during three large coronal mass ejection-driven storms, microbursts during the main phase contributed significant losses to the outer radiation belt while those in the recovery phase were of smaller magnitude and contributed orders of magnitude less loss than the main phase microbursts. This suggests that microburst magnitude may be dependent not only upon storm phase but also upon storm type. The similar microburst magnitudes between the main and recovery phases, combined with increased occurrence rates in the recovery phase, indicate that either additional main phase losses or strong recovery phase acceleration must also be occurring, to compensate for microburst losses in the recovery phases of HSS-driven storms.
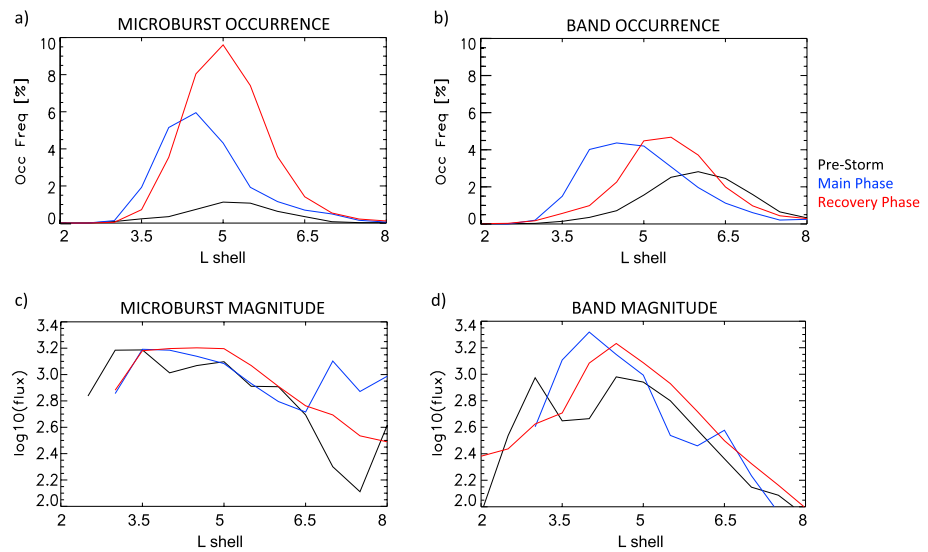
Figure 6. Occurrence rates of (a) microbursts and (b) precipitation bands as a function of L shell during the prestorm (black), main phase (blue), and recovery phase (red) of 42 HSS-driven storms. Precipitation magnitudes are shown for (c) microbursts and (d) precipitation bands, respectively.

On average, precipitation bands show a slight increase in occurrence right around zero epoch, up to ~3.2% from a prestorm, quiet time value around 1.2% (Figure 5a). This increase occurs at L shells of 4–5 (black and red, respectively, in Figure 5c) and coincides with the time of observed dropouts in trapped radiation belt fluxes during HSS-driven storms. Occurrence rates at L = 5.5–6.5 (blue line, Figure 5c) actually show a decrease just after this time, which is likely due to the general inward motion of all the precipitation features around zero epoch. The magnitudes of precipitation bands also increase beginning roughly 0.5 h before zero epoch, as shown in Figures 5b, 5d, and 6d. These magnitudes peak at values around $10^{3.3}$ (MeV cm^2 sr s)$^{-1}$ right at zero epoch at the inner edge of the outer radiation belt, around L = 4, and drop off as one moves radially outward. The observed increase in precipitation band occurrence rate and magnitude at the inner edge of the outer radiation belt around zero epoch is consistent with enhanced EMIC wave activity during this time, as suggested by *Borovsky and Denton* [2009a] as well as *MacDonald et al.* [2010], and suggests that this mechanism may play a role, especially at low L shells, in the main phase losses observed throughout the outer belt. At larger L shells, however, precipitation band magnitudes and occurrence rates do not vary dramatically with storm phase (see Figures 6b and 6d), suggesting that additional loss processes are needed to explain dropouts observed at geosynchronous orbit. Studies have shown that radiation belt losses through outward radial diffusion and magnetopause shadowing can produce significant radiation belt depletions [*Shprits et al.*, 2006; *Turner et al.*, 2012]; however, these mechanisms often cannot fully account for losses observed at lower L shells, within L ~ 5 [*Hudson et al.*, 2014; *Turner et al.*, 2014]. These SAMPEX observations provide strong evidence for atmospheric precipitation at the inner edge of the outer radiation belt, which, in combination with other losses such as those to the magnetopause, may explain observed dropouts across the outer radiation belt during HSS-driven storms.

Finally, Figures 6a and 6b display the occurrence rates of microbursts and precipitation bands, respectively, as a function of L shell, averaged over three phases of the HSS-driven storms. An increase in the occurrence of both these precipitation types occurs in the main and recovery phases, revealing MeV electron precipitation that is not fully captured by POES spacecraft during these events. POES Medium Energy Proton and Electron Detector (MEPED) has three electron channels, >30 keV, >100 keV, and >300 keV [*Evans and Greer*, 2004]. However, its highest-energy proton channel has been shown to be sensitive to electrons > ~1 MeV [*Yando et al.*, 2011] and is thus often used for radiation belt studies during times when solar proton events are not occurring. The MEPED instrument consists of two 30° field of view telescopes, one looking roughly along the field line (0° or T0) and one looking perpendicular (90° or T90). At latitudes mapping to the outer radiation belt, the 90° telescope responds to trapped and drift loss cone electrons while the 0° telescope

measures precipitating electrons. However, with its 30° field of view, the 0° telescope covers only a small fraction of the total loss cone, anywhere from 2 to 10% [*Hendry et al.*, 2012]. Additionally, count rates have 2 s resolution, so POES is not able to detect more rapid microburst precipitation. Thus, the large field of view and geometric factor combined with high time resolution of SAMPEX/HILT are able to reveal enhanced precipitation loss at a variety of timescales occurring during HSS-driven storms.

5. Summary

Here we use high time resolution SAMPEX/HILT measurements to study rapid precipitation events, their spatial distributions, and their relation to storm time radiation belt dynamics. Millisecond-long microbursts, as well as longer-duration precipitation bands, are investigated across a set of high-speed stream-driven storms with the aim of understanding the relative role of these two loss processes. This work investigates not only when precipitation is occurring but also what type of precipitation it is, allowing the contributions of different scattering mechanisms to overall radiation belt dynamics to be studied independently. Our results are summarized as follows:

1. Microburst occurrence rates increase in the recovery phase of HSS-driven storms, concurrent with rebuilding of the outer radiation belt and consistent with chorus as both a loss and an acceleration mechanism. Microburst magnitudes exhibit little variation with storm phase during these events, however. Together, these distributions suggest that microburst recovery phase losses may be as or more significant than those in the main phase and must be compensated for by concurrent acceleration mechanisms.
2. Precipitation bands increase in magnitude and occurrence during the main phase of HSS storms, particularly toward the inner edge of the outer radiation belt, suggesting that atmospheric losses to the duskside magnetosphere play a role in MeV electron dropouts at low L shells. Their occurrences and magnitudes at larger L shells (L≥∼6), however, do not show significant storm phase dependence, suggesting that additional loss mechanisms are needed to produce dropouts observed at geostationary orbit.
3. SAMPEX/HILT observes enhanced precipitation, both microburst and band type, during the main and recovery phases of HSS-driven storms. The large geometric factor, wide field of view, and high time resolution of SAMPEX/HILT reveal the contribution of these rapid precipitation features to storm time radiation belt dynamics.

References

Albert, J. M. (2003), Evaluation of quasi-linear diffusion coefficients for EMIC waves in a multispecies plasma, *J. Geophys. Res.*, *108*(A6), 1249, doi:10.1029/2002JA009792.

Anderson, K. A., and D. W. Milton (1964), Balloon observations of X-rays in the auroral zone, *J. Geophys. Res.*, *69*, 551–564.

Baker, D. N., G. M. Mason, O. Figueroa, G. Colon, J. G. Watzin, and R. M. Aleman (1993), An overview of the Solar Anomalous, and Magnetospheric Particle Explorer (SAMPEX) mission, *Geosci. Remote Sens. IEEE Trans.*, *31*(3), 531–541.

Baker, D. N., J. E. Mazur, and G. Mason (2012), SAMPEX to reenter atmosphere: Twenty-year mission will end, *Space Weather*, *10*, S05006, doi:10.1029/2012SW000804.

Blake, J. B., M. D. Looper, D. N. Baker, R. Nakamura, B. Klecker, and D. Hovestadt (1996), New high temporal and spatial resolution measurements by SAMPEX of the precipitation of relativistic electrons, *Adv. Space Res.*, *18*, 171–186.

Blum, L. W., Q. Schiller, X. Li, R. Millan, A. Halford, and L. Woodger (2013), New conjunctive CubeSat and balloon measurements to quantify rapid energetic electron precipitation, *Geophys. Res. Lett.*, *40*, 5833–5837, doi:10.1002/2013GL058546.

Borovsky, J. E., and M. H. Denton (2009a), Relativistic-electron dropouts and recovery: A superposed epoch study of the magnetosphere and the solar wind, *J. Geophys. Res.*, *114*, A02201, doi:10.1029/2008JA013128.

Borovsky, J. E., and M. H. Denton (2009b), Electron loss rates from the outer radiation belt caused by the filling of the outer plasmasphere: The calm before the storm, *J. Geophys. Res.*, *114*, A11203, doi:10.1029/2009JA014063.

Bortnik, J., and R. M. Thorne (2007), The dual role of ELF/VLF chorus waves in the acceleration and precipitation of radiation belt electrons, *J. Atmos. Sol. Terr. Phys.*, *69*, 378–386, doi:10.1016/j.jastp.2006.05.030.

Bortnik, J., R. M. Thorne, T. P. O'Brien, J. C. Green, R. J. Strangeway, Y. Y. Shprits, and D. N. Baker (2006), Observation of two distinct, rapid loss mechanisms during the 20 November 2003 radiation belt dropout event, *J. Geophys. Res.*, *111*, A12216, doi:10.1029/2006JA011802.

Bossen, M., R. L. McPherron, and C. T. Russell (1976), A statistical study of Pc 1 magnetic pulsations at synchronous orbit, *J. Geophys. Res.*, *81*, 6083–6091, doi:10.1029/JA081i034p06083.

Brown, J. W., and E. C. Stone (1972), High-energy electron spikes at high latitudes, *J. Geophys. Res.*, *77*, 3384–3396.

Carpenter, D. L., and R. R. Anderson (1992), An ISEE/whistler model of equatorial electron density in the magnetosphere, *J. Geophys. Res.*, *97*, 1097–1108, doi:10.1029/91JA01548.

Carson, B. R., C. J. Rodger, and M. A. Clilverd (2013), POES satellite observations of EMIC-wave driven relativistic electron precipitation during 1998–2010, *J. Geophys. Res. Space Physics*, *118*, 232–243, doi:10.1029/2012JA017998.

Cattell, C., et al. (2008), Discovery of very large amplitude whistler-mode waves in Earth's radiation belts, *Geophys. Res. Lett.*, *35*, L01105, doi:10.1029/2007GL032009.

Clausen, L. B. N., J. B. H. Baker, J. M. Ruohoniemi, and H. J. Singer (2011), EMIC waves observed at geosynchronous orbit during solar minimum: Statistics and excitation, *J. Geophys. Res.*, *116*, A10205, doi:10.1029/2011JA016823.

Clilverd, M. A., et al. (2009), Remote sensing space weather events: The AARDDVARK network, *Space Weather*, 7, S04001, doi:10.1029/2008SW000412.

Comess, M. D., D. M. Smith, R. S. Selesnick, R. M. Millan, and J. G. Sample (2013), Duskside relativistic electron precipitation as measured by SAMPEX: A statistical survey, *J. Geophys. Res. Space Physics*, 118, 5050–5058, doi:10.1002/jgra.50481.

Denton, M. H., and J. E. Borovsky (2008), Superposed epoch analysis of high-speed-stream effects at geosynchronous orbit: Hot plasma, cold plasma, and the solar wind, *J. Geophys. Res.*, 113, A07216, doi:10.1029/2007JA012998.

Denton, M. H., J. E. Borovsky, and T. E. Cayton (2010), A density-temperature description of the outer radiation belt during geomagnetic storms, *J. Geophys. Res.*, 115, A01208, doi:10.1029/2009JA014183.

Dietrich, S., C. J. Rodger, M. A. Clilverd, J. Bortnik, and T. Raita (2010), Relativistic microbursts storm characteristics: Combined satellite and ground-based observations, *J. Geophys. Res.*, 115, A12240, doi:10.1029/2010JA015777.

Evans, D. S., and M. S. Greer (2004), Polar Orbiting Environmental Satellite Space Environment Monitor—2. Instrument descriptions and archive data documentation, version 2.0, technical memorandum, Space Environ. Lab., NOAA, Boulder, Colo. [Available at http://ngdc.noaa.gov/stp/satellite/poes/documentation.html.]

Foat, J. E., R. P. Lin, D. M. Smith, F. Fenrich, R. Millan, I. Roth, K. R. Lorentzen, M. P. McCarthy, G. K. Parks, and J. P. Treilhou (1998), First detection of a terrestrial MeV X-ray burst, *Geophys. Res. Lett.*, 25, 4109–4112, doi:10.1029/1998GL900134.

Fraser, B. J., and T. S. Nguyen (2001), Is the plasmapause a preferred source region of electromagnetic ion cyclotron waves in the magnetosphere?, *J. Atmos. Sol. Terr. Phys.*, 63, 1225–1247, doi:10.1016/S1364-6826(00)00225-X.

Friedel, R. H. W., G. D. Reeves, and T. Obara (2002), Relativistic electron dynamics in the inner magnetosphere—A review, *J. Atmos. Sol. Terr. Phys.*, 64, 265.

Goldstein, J., R. A. Wolf, B. R. Sandel, W. T. Forrester, D. L. Gallagher, P. H. Reiff, and R. Spiro (2002), Rapid response of the plasmasphere to changes in the solar wind and IMF: Global plasmapause electric field measurements by IMAGE EUV, and simulation with the Rice MSM, *Eos Trans. AGU*, 83(19Spring Meet. Suppl., SM41B-09).

Halford, A. J., B. J. Fraser, and S. K. Morley (2010), EMIC wave activity during geomagnetic storm and nonstorm periods: CRRES results, *J. Geophys. Res.*, 115, A12248, doi:10.1029/2010JA015716.

Hendry, A. T., C. J. Rodger, M. A. Clilverd, N. R. Thomson, S. K. Morley, and T. Raita (2012), Rapid radiation belt losses occurring during high-speed solar wind stream-driven storms: Importance of energetic electron precipitation, in *Dynamics of the Earth's Radiation Belts and Inner Magnetosphere*, Geophys. Monogr. Ser., vol. 199, edited by D. Summers et al., pp. 213–223, AGU, Washington, D. C., doi:10.1029/2012GM001299.

Horne, R. B., and R. M. Thorne (2003), Relativistic electron acceleration and precipitation during resonant interactions with whistler-mode chorus, *Geophys. Res. Lett.*, 30(10), 1527, doi:10.1029/2003GL016973.

Hudson, M. K., D. N. Baker, J. Goldstein, B. T. Kress, J. Paral, F. R. Toffeletto, and M. Wiltberger (2014), Simulated magnetopause losses and Van Allen Probe flux dropouts, *Geophys. Res. Lett.*, 41, 1113–1118, doi:10.1002/2014GL059222.

Imhof, W. L., H. D. Voss, J. B. Reagan, D. W. Datlowe, E. E. Gaines, and J. Mobilia (1986), Relativistic electron and energetic ion precipitation spikes near the plasmapause, *J. Geophys. Res.*, 91, 3077–3088, doi:10.1029/JA091iA03p03077.

Imhof, W. L., H. D. Voss, J. Mobilia, D. W. Datlowe, and E. E. Gaines (1991), The precipitation of relativistic electrons near the trapping boundary, *J. Geophys. Res.*, 96, 5619–5629, doi:10.1029/90JA02343.

Imhof, W. L., R. M. Robinson, H. L. Collin, J. R. Wygant, and R. R. Anderson (1992), Simultaneous equatorial measurements of waves and precipitating electrons in the outer radiation belt, *Geophys. Res. Lett.*, 19, 2437–2440, doi:10.1029/92GL02636.

Johnston, W. R., and P. C. Anderson (2010), Storm time occurrence of relativistic electron microbursts in relation to the plasmapause, *J. Geophys. Res.*, 115, A02205, doi:10.1029/2009JA014328.

Kersten, K., C. A. Cattell, A. Breneman, K. Goetz, P. J. Kellogg, J. R. Wygant, L. B. Wilson, J. B. Blake, M. D. Looper, and I. Roth (2011), Observation of relativistic electron microbursts in conjunction with intense radiation belt whistler-mode waves, *Geophys. Res. Lett.*, 38, L08107, doi:10.1029/2011GL046810.

Klecker, B., D. Hovestadt, M. Sholer, H. Arbinger, M. Ertl, H. Kastle, E. Kunneth, P. Laeverenz, and E. Seidenschwang (1993), "HILT: A Heavy Ion Large Proportional Counter Telescope for solar and anomalous cosmic rays," *IEEE Trans. Geosci. Remote Sens.*, 31, 542–548.

Koons, H. C., A. L. Vampola, and D. A. McPherson (1972), Strong pitch-angle scattering of energetic electrons in the presence of electrostatic waves above the ionospheric trough region, *J. Geophys. Res.*, 77, 1771–1775, doi:10.1029/JA077i010p01771.

Li, X., and M. Temerin (2001), The electron radiation belt, *Space Sci. Rev.*, 96(1–2), doi:10.1023/A:1005221108016.

Li, X., D. N. Baker, M. Temerin, D. Larson, R. P. Lin, E. G. D. Reeves, M. D. Looper, S. G. Kanekal, and R. A. Mewaldt (1997a), Are energetic electrons in the solar wind the source of the outer radiation belt?, *Goephys. Res. Lett.*, 24, 923–926.

Li, X., D. Baker, M. Temerin, T. E. Cayton, E. G. D. Reeves, R. A. Christensen, J. B. Blake, M. D. Looper, R. Nakamura, and S. G. Kanekal (1997b), Multisatellite observations of the outer zone electron variation during the November 3–4, 1993, magnetic storm, *J. Geophys. Res.*, 102, 14,123–14,140, doi:10.1029/97JA01101.

Liemohn, M. W., and A. A. Chan (2007), Unraveling the causes of radiation belt enhancements, *Eos Trans. AGU*, 88(42), 425–426, doi:10.1029/2007EO420001.

Lorentzen, K. R., J. B. Blake, U. S. Inan, and J. Bortnik (2001), Observations of relativistic electron microbursts in association with VLF chorus, *J. Geophys. Res.*, 106, 6017–6027, doi:10.1029/2000JA003018.

MacDonald, E. A., L. W. Blum, S. P. Gary, M. F. Thomsen, and M. H. Denton (2010), High-speed stream driven inferences of global wave -distributions at geosynchronous orbit: Relevance to radiation-belt dynamics, *Proc. R. Soc. A*, 466, 3351–3362, doi:10.1098/rspa.2010.0076.

Madden, D., and M. S. Gussenhoven (1990), Auroral boundary index from 1983 to 1990, Tech. Rep. GL-TR-90-0358, Air Force Geophys. Lab., Hanscom AFB, Mass.

McCollough, J. P., S. R. Elkington, and D. N. Baker (2012), The role of Shabansky orbits in compression-related electromagnetic ion cyclotron wave growth, *J. Geophys. Res.*, 117, A01208, doi:10.1029/2011JA016948.

Meredith, N. P., R. M. Thorne, R. B. Horne, D. Summers, B. J. Fraser, and R. R. Anderson (2003), Statistical analysis of relativistic electron energies for cyclotron resonance with EMIC waves observed on CRRES, *J. Geophys. Res.*, 108(A6), 1250, doi:10.1029/2002JA009700.

Meredith, N. P., R. B. Horne, S. A. Glauert, R. M. Thorne, D. Summers, J. M. Albert, and R. R. Anderson (2006), Energetic outer zone electron loss timescales during low geomagnetic activity, *J. Geophys. Res.*, 111, A05212, doi:10.1029/2005JA011516.

Meredith, N. P., R. B. Horne, M. M. Lam, M. H. Denton, J. E. Borovsky, and J. C. Green (2011), Energetic electron precipitation during high-speed solar wind stream driven storms, *J. Geophys. Res.*, 116, A05223, doi:10.1029/2010JA016293.

Millan, R. M., and R. M. Thorne (2007), Review of radiation belt relativistic electron losses, *J. Atmos. Sol. Terr. Phys.*, 69, 362–377.

Millan, R. M., R. P. Lin, D. M. Smith, K. R. Lorentzen, and M. P. McCarthy (2002), X-ray observations of MeV electron precipitation with a balloon-borne germanium spectrometer, *Geophys. Res. Lett.*, 29(24), 2194, doi:10.1029/2002GL015922.

Millan, R. M., R. P. Lin, D. M. Smith, and M. P. McCarthy (2007), Observations of relativistic electron precipitation during a rapid decrease of trapped relativistic electron flux, *Geophys. Res. Lett.*, *34*, L10101, doi:10.1029/2006GL028653.

Miyoshi, Y., and R. Kataoka (2008), Flux enhancement of the outer radiation belt electrons after the arrival of stream interaction regions, *J. Geophys. Res.*, *113*, A03S09, doi:10.1029/2007JA012506.

Miyoshi, Y., K. Sakaguchi, K. Shiokawa, D. Evans, J. Albert, M. Connors, and V. Jordanova (2008), Precipitation of radiation belt electrons by EMIC waves, observed from ground and space, *Geophys. Res. Lett.*, *35*, L23101, doi:10.1029/2008GL035727.

Morley, S. K., R. H. W. Friedel, E. L. Spanswick, G. D. Reeves, J. T. Steinberg, J. Koller, T. Cayton, and E. Noveroske (2010), Dropouts of the outer electron radiation belt in response to solar wind stream interfaces: Global Positioning System observations, *Proc. R. Soc. A*, *466*(2123), 3329–3350.

Nakamura, R., M. Isowa, Y. Kamide, D. N. Baker, J. B. Blake, and M. Looper (2000), SAMPEX observations of precipitation bursts in the outer radiation belt, *J. Geophys. Res.*, *105*, 15,875–15,885, doi:10.1029/2000JA900018.

O'Brien, T. P., K. R. Lorentzen, I. R. Mann, N. P. Meredith, J. B. Blake, J. F. Fennel, M. D. Looper, D. K. Milling, and R. R. Anderson (2003), Energization of relativistic electrons in the presence of ULF wave power and MeV microbursts: Evidence for dual ULF and VLF acceleration, *J. Geophys. Res.*, *108*(A8), 1329, doi:10.1029/2002JA009784.

O'Brien, T. P., M. D. Looper, and J. B. Blake (2004), Quantification of relativistic electron microburst losses during the GEM storms, *Geophys. Res. Lett.*, *31*, L04802, doi:10.1029/2003GL018621.

Reeves, G. D., K. L. McAdams, R. H. W. Friedel, and T. P. O'Brien (2003), Acceleration and loss of relativistic electrons during geomagnetic storms, *Geophys. Res. Lett.*, *30*(10), 1529, doi:10.1029/2002GL016513.

Saito, S., Y. Miyoshi, and K. Seki (2012), Relativistic electron microbursts associated with whistler chorus rising tone elements: GEMSIS-RBW simulations, *J. Geophys. Res.*, *117*, A10206, doi:10.1029/2012JA018020.

Sandanger, M., F. Søraas, K. Aarsnes, K. Oksavik, and D. S. Evans (2007), Loss of relativistic electrons: Evidence for pitch angle scattering by electromagnetic ion cyclotron waves excited by unstable ring current protons, *J. Geophys. Res.*, *112*, A12213, doi:10.1029/2006JA012138.

Sandanger, M., F. Søraas, M. Sørbø, K. Aarsnes, K. Oksavik, and D. S. Evans (2009), Relativistic electron losses related to EMIC waves during CIR and CME storms, *J. Atmos. Sol. Terr. Phys.*, *71*, 1126–1144, doi:10.1016/j.jastp.2008.07.006.

Shklyar, D. R., and B. Kliem (2006), Relativistic electron scattering by electrostatic upper hybrid waves in the radiation belt, *J. Geophys. Res.*, *111*, A06204, doi:10.1029/2005JA011345.

Shprits, Y. Y., et al. (2006), Outward radial diffusion driven by losses at magnetopause, *J. Geophys. Res.*, *111*, A11214, doi:10.1029/2006JA011657.

Spasojevic, M., H. U. Frey, M. F. Thomsen, S. A. Fuselier, S. P. Gary, B. R. Sandel, and U. S. Inan (2004), The link between a detached subauroral proton arc and a plasmaspheric plume, *Geophys. Res. Lett.*, *31*, L04803, doi:10.1029/2003GL018389.

Spence, H. E., et al. (2012), Focusing on size and energy dependence of electron microbursts from the Van Allen radiation belts, *Space Weather*, *10*, S11004, doi:10.1029/2012SW000869.

Summers, D., and R. M. Thorne (2003), Relativistic electron pitch-angle scattering by electromagnetic ion cyclotron waves during geomagnetic storms, *J. Geophys. Res.*, *108*(A4), 1143, doi:10.1029/2002JA009489.

Thorne, R. M., and C. F. Kennel (1971), Relativistic electron precipitation during magnetic storm main phase, *J. Geophys. Res.*, *76*, 4446–4453, doi:10.1029/JA076i019p04446.

Thorne, R. M., T. P. O'Brien, Y. Y. Shprits, D. Summers, and R. B. Horne (2005), Timescale for MeV electron microburst loss during geomagnetic storms, *J. Geophys. Res.*, *110*, A09202, doi:10.1029/2004JA010882.

Tsurutani, B. T., and E. J. Smith (1977), Two types of magnetospheric ELF chorus and their substorm dependences, *J. Geophys. Res.*, *82*, 5112–5128, doi:10.1029/JA082i032p05112.

Turner, D. L., Y. Y. Shprits, M. Hartinger, and V. Angelopoulos (2012), Explaining sudden losses of outer radiation belt electrons during geomagnetic storms, *Nat. Phys.*, *8*, 208–212, doi:10.1038/NPHYS2185.

Turner, D. L., et al. (2014), On the cause and extent of outer radiation belt losses during the 30 September 2012 dropout event, *J. Geophys. Res. Space Physics*, *119*, 1530–1540, doi:10.1002/2013JA019446.

Usanova, M. E., I. R. Mann, J. Bortnik, L. Shao, and V. Angelopoulos (2012), THEMIS observations of electromagnetic ion cyclotron wave occurrence: Dependence on AE, SYMH, and solar wind dynamic pressure, *J. Geophys. Res.*, *117*, A10218, doi:10.1029/2012JA018049.

Vampola, A. L. (1971), Electron pitch angle scattering in the outer zone during magnetically disturbed times, *J. Geophys. Res.*, *76*, 4685–4688, doi:10.1029/JA076i019p04685.

Vampola, A. L. (1977), The effect of strong pitch angle scattering on the location of the outer-zone electron boundary as observed by low-altitude satellites, *J. Geophys. Res.*, *82*, 2289–2294, doi:10.1029/JA082i016p02289.

Yando, K., R. M. Millan, J. C. Green, and D. S. Evans (2011), A Monte Carlo simulation of the NOAA POES Medium Energy Proton and Electron Detector instrument, *J. Geophys. Res.*, *116*, A10231, doi:10.1029/2011JA016671.